

Suppressing quasiparticle poisoning with a voltage-controlled filterGerbold C. Ménard,^{1,*} Filip K. Malinowski,^{1,*} Denise Puglia,¹ Dmitry I. Pikulin,² Torsten Karzig,² Bela Bauer,² Peter Krogstrup,³ and Charles M. Marcus¹¹*Center for Quantum Devices, Niels Bohr Institute, University of Copenhagen and Microsoft Quantum Lab, Universitetsparken 5, 2100 Copenhagen, Denmark*²*Microsoft Station Q, University of California, Santa Barbara, California 93106-6105, USA*³*Microsoft Quantum Materials Lab, Kanalvej 7, 2800 Lyngby, Denmark*

(Received 7 February 2019; revised manuscript received 24 July 2019; published 29 October 2019)

We study single-electron charging events in an Al/InAs nanowire hybrid system with deliberately introduced gapless regions. The occupancy of a Coulomb island is detected using a nearby radio-frequency quantum dot as a charge sensor. We demonstrate that a 1- μm -long gapped segment of the wire can be used to efficiently suppress single electron poisoning of the gapless region and therefore protect the parity of the island while maintaining good electrical contact with a normal lead. In the absence of protection by charging energy, the $1e$ switching rate can be reduced below $\Gamma = 200 \text{ s}^{-1}$. In the same configuration, we observe strong quantum charge fluctuations due to the exchange of electron pairs between the island and the lead. The magnetic-field dependence of the poisoning rate yields a zero-field superconducting coherence length of $\xi = 90 \pm 10 \text{ nm}$.

DOI: [10.1103/PhysRevB.100.165307](https://doi.org/10.1103/PhysRevB.100.165307)**I. INTRODUCTION**

Semiconductor-superconductor hybrids combine coherence effects at the macroscopic scale (superconductors) with the ease of tuning by means of electric and magnetic fields (semiconductors). An ever-growing class of phenomena enabled by these hybrids include quantum phase transitions [1] such as superconductor-insulator transition [2–4] or topological superconducting transitions [5–13]. Furthermore, such structures are at the heart of qubit designs such as gate-tunable transmon [14–17] and proposed topological Majorana qubits [18–20].

One cause for dephasing and relaxation in superconducting qubits is quasiparticle poisoning [21–27]. It occurs in both conventional superconducting qubits [28–32] and hybrid supersemiconducting qubits [15–17]. In the latter case, the induced superconducting gap in the semiconducting part of the heterostructure is reduced [33–35] and thereby they are more susceptible to poisoning.

This paper describes a method that can significantly reduce the detrimental effects of quasiparticle poisoning. Specifically, we introduce a tunable quasiparticle filter made from an InAs nanowire with an epitaxial aluminum shell on two facets [36–38]. Such a component can provide an electrical connection, with Cooper pairs as charge carriers, while keeping quasiparticle transport to a minimum between two ungapped segments of the device: One that is poisoned and another that needs to remain in a fixed parity state.

An example of systems that are in need of a quasiparticle filter are Majorana-based topological qubits [18,19]. Proposed designs of such a qubit commonly require large-scale (potentially strongly poisoned) superconducting networks

compatible with high magnetic fields and connected to non-superconducting leads, as well as smaller regions of topological superconductor-hosting Majorana zero modes, which decohere as a result of the poisoning [26,39,40].

The devices under study consist of two gapless regions (metallic lead and soft-gapped proximitized nanowire) separated by a clean InAs nanowire segment with an epitaxial aluminum shell [36–38] with a tunable gap [41,42]. To enable charge detection, the clean InAs/Al and soft-gapped regions are configured as a single island (i.e., a quantum dot). By means of radio-frequency charge sensing with microsecond temporal resolution [43–48], we observe single-electron tunneling events between two zero-gapped regions while tuning the superconducting gap of the filter by electrostatic gating and applied magnetic field. Increasing the coupling of the semiconductor part of the clean nanowire segment to the superconductor, resulting in the hard gap, suppresses the single-electron tunneling events between the zero-gapped regions, yielding a poisoning rate of $\Gamma_{\text{on}} = 151 \pm 26 \text{ s}^{-1}$. At the same time, the island remains strongly coupled to the lead as revealed by observed quantum charge fluctuations. This study can be effectively viewed as an exploration of the intermediate regime, between poisoning studies of islands directly coupled to the normal leads [25] (zero-length filter limit) and islands coupled to macroscopic superconducting leads [22] (infinite-length filter limit) and indeed finds the poisoning rates on the intermediate timescale.

This paper is organized as follows. Section II presents the description of the devices and methods. Section III is dedicated to the characterization of the device using conventional lock-in techniques and radio-frequency measurements. Section IV introduces charge stability diagrams of the studied island. Section V describes the specific measurement and analysis protocols used to quantify the quasiparticle poisoning rate. In Sec. VI, we use these protocols to perform

*These authors contributed equally to this paper.

an analysis of the quasiparticle poisoning rate as a function of gate voltages and external magnetic field. Section VII demonstrates evidence of quantum charge fluctuations in the device configuration characterized by low poisoning rates. Finally, a summary of findings and potential applications of the quasiparticle nanowire filter are presented in Sec. VIII.

II. DEVICE AND EXPERIMENTAL METHODS

The study was performed on two lithographically similar devices, illustrated in Fig. 1. In the following, we specify in the caption of each figure for which of the two devices (A or B) the corresponding data set was obtained. We first describe their structures from the fabrication perspective and later discuss the purpose that each element serves in our experiment.

The devices are based on an InAs nanowire with a 2-nm-thick MBE-grown Al shell on two facets [36]. The nanowire is placed on a SiO₂ insulating substrate, and the metallic contacts and gates are deposited using e-beam lithography. The nanowire is contacted by three Ti/Au leads [colored in red in Fig. 1(a)], deposited after local wet etching of the Al shell using Transcene D and Ar milling to obtain ohmic contact with the semiconductor. Blue-colored 150 nm NbTiN is in electrical contact with the wire. In the case of device A, NbTiN is covered by 5 nm of gold, intended as a quasiparticle trap. In the case of device B, the NbTiN is

left as is and no gold was deposited. The nanowire, ohmic contacts, and NbTiN/(Au) structure are covered by 7 nm of ALD-grown HfO₂. We deposit additional Ti/Au gates on top of the oxide layer. The voltage on yellow-colored gates is controlled, while the gray-colored gate is electrically floating. We didn't observe a significant difference in the behavior of device A and B, indicating that the Au played no role in the poisoning process.

The device consists of two islands defined in the Al-covered nanowire. In the experiment, we study $1e$ charging rates of the larger, left island, detected using the small, right island as a charge sensor [43–48]. Charge sensing is enhanced by means of a floating gate which increases the capacitive coupling between the two islands.

The main (left) island consists of two different parts. The first one, labeled $1e$ region in Fig. 1(b), is connected to the blue-colored NbTiN structure. This segment is gapless due to at least one of these effects: The choice of the gate voltage V_G for which weakly proximitized states in the semiconductor are highly populated [42], the softness of the superconducting gap observed in structures including NbTiN [22,49,50], the damaged interface of the nanowire that was milled to obtain an electrical contact to the NbTiN and, in case of device A, gold quasiparticle traps evaporated on top of the NbTiN structure.

The second part of the quantum dot, labeled filter in Fig. 1(b), is a nanowire covered by epitaxial Al. By applying a voltage V_F to the neighboring gate, the coupling between the semiconducting wire and the superconducting shell in the segment can be tuned, effectively tuning a subgap density of states [41,42,51] in a form of gap-engineering [52]. The Al shell of the nanowire is continuous throughout the island, which prevents the creation of an unintentional barrier dividing a single island in two.

The main island ($1e$ region and filter) is connected via gateable barriers to two normal-metal leads, one neighboring the $1e$ region, the other neighboring the filter. Adjusting barrier gate voltages V_L and V_R allows us to tune the barriers to the two leads from open regime (conductance through the barrier $> 2 e^2/h$) to tunneling regime (conductance $\simeq 0.5 e^2/h$) to fully closed (tunneling times of minutes or longer).

The device is designed to mimic scalable designs for Majorana-based quantum computation [19,20]. In particular, the $1e$ region emulates a topologically trivial superconductor contacting the proximitized nanowire through a rough interface that may be a source of quasiparticles. The right normal lead mimics a topological region, at the end of which there are low-energy bound states. Finally, the filter is intended to prevent the quasiparticle tunneling between the two regions, thereby protecting the parity of the bound states.

Measurements are performed using several techniques. The differential conductance through the main island can be measured using standard lock-in techniques. Alternatively, a radio-frequency resonant circuit connected to the central lead (indicated by a coil symbol in Fig. 1) is also used to perform an effective differential conductance measurement through the main or sensor island, by using rf reflectometry combined with analog homodyne demodulation. When conductance through the sensor island is suppressed, reflectometry can be used as a substitute for lock-in measurements [47]. Finally, when conductance through the main island is suppressed and

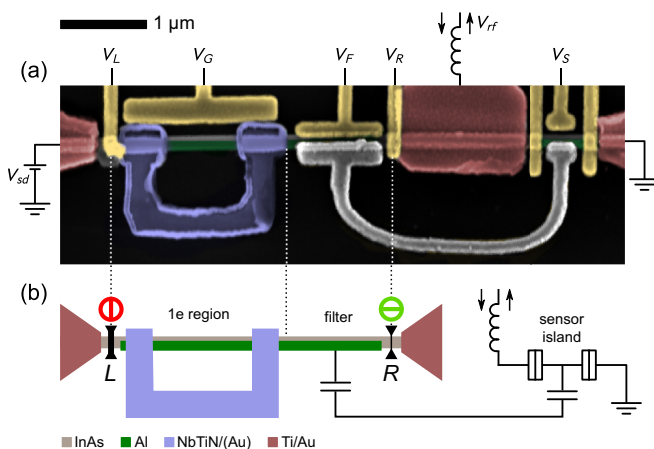


FIG. 1. (a) Colorized scanning electron micrograph of one of the devices under investigation. The devices are based on an InAs nanowire (dark-grey) with epitaxial aluminum shell on two of the six facets (green). The aluminum shell is nominally 5 nm thick, but due to oxidation in contact with air we expect it to be effectively 2–3 nm thick. Red-colored regions are Ti/Au ohmic contacts. Gates are used to define and control occupancy of the two islands (yellow). NbTiN/(Au) structure (blue) emulates complex high-field-compatible superconducting network. Capacitive coupling between the islands is enhanced by a floating metallic bridge (white colored). (b) Simplified schematic of the device. During the key measurements, the barrier connecting the large island to the lead on the left side L is fully pinched off, preventing any tunneling events on a minute timescale, meanwhile the right barrier R is operated in the tunneling regime. The smaller island is operated as a rf charge sensor. The 40 MHz LC resonant circuit is indicated by a coil symbol.

the sensor island is tuned to the slope of the Coulomb peak, the charge on the main island can be detected with microsecond temporal resolution.

The experiment was performed in a dilution refrigerator equipped with a vector superconducting magnet. The mixing chamber plate of the refrigerator was at base temperature of 20 mK and, unless mentioned otherwise, no magnetic field was applied.

III. LOW-FREQUENCY CHARACTERIZATION

We first characterize the main island in our device using standard lock-in techniques or equivalent reflectometry

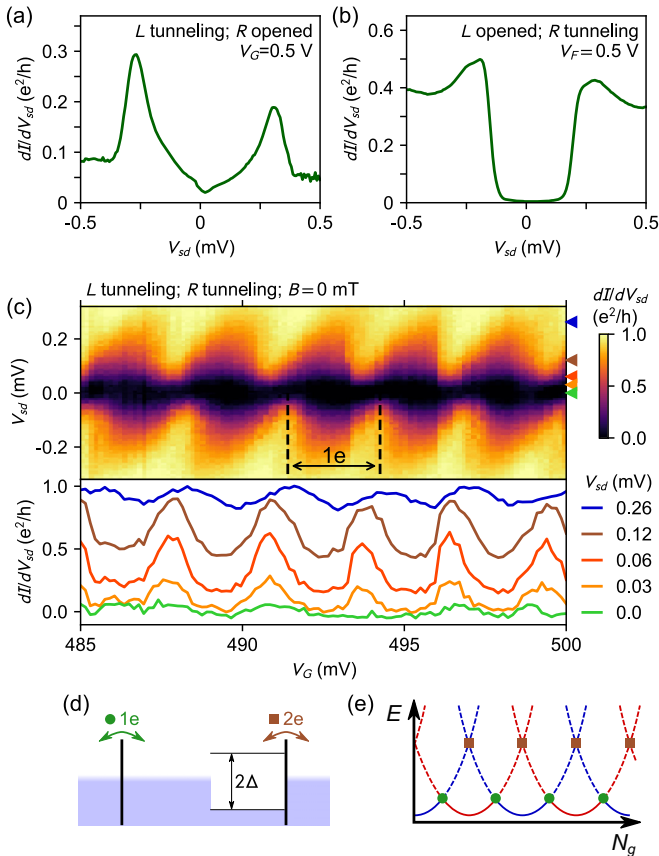


FIG. 2. Tunneling spectroscopy of the superconducting gap at the left (a) and right (b) end of the main island obtained using lock-in techniques. The inset text indicates the status of the left (L) and right (R) barriers. (c) Coulomb diamonds with very strongly suppressed zero bias conductance obtained by reflectometry measurements converted to conductance. Bottom panel shows cuts through the data at various V_{sd} . (d) Schematics illustrating that in an island configuration the right barrier only enables exchange of electron pairs with the lead, while the left barrier also facilitates the exchange of single electrons. (e) Energy of different island occupancies as a function of the gate-induced charge. Brown squares indicate the degeneracy point at which $2e$ transport through the right barrier may occur. This point is never reached, since at the points indicated by the green circles the single electron is exchanged via the left barrier, enabling the island to remain in the ground state (solid lines). Data for device A.

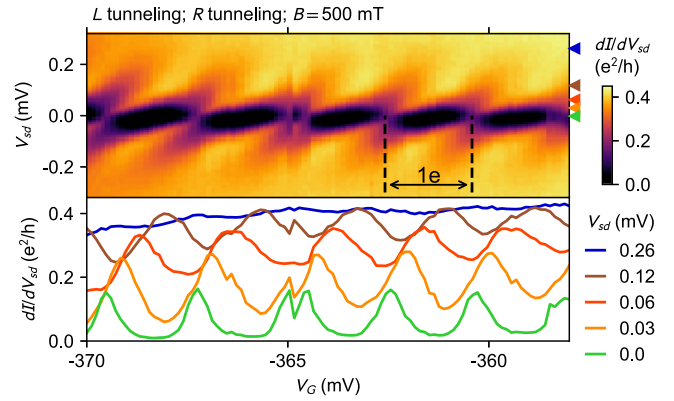


FIG. 3. Coulomb diamonds at $B = 500$ mT, in plane of the sample, not parallel to the nanowire, obtained by lock-in techniques. No conductance suppression occurs at low V_{sd} , as exemplified with the cuts presented in the bottom panel. Data for device A.

measurements [47]. Figure 2 summarizes our findings for zero external magnetic field.

Figures 2(a) and 2(b) characterize the superconducting gap of the $1e$ region and the filter, respectively, by means of tunneling spectroscopy. The tunneling spectroscopy on the left end of the main island reveals a soft gap. In contrast, the right end of the island shows a hard gap. Similar data is shown in Appendix C for the other device. We gain further insight into the properties of the $1e$ region and the filter region in the Coulomb-diamond measurements presented in Fig. 2(c). We find that a zero bias conductance through the island is strongly suppressed as emphasized by the cuts at different bias values V_{sd} , presented in the bottom panel. The zero-bias suppression of conductance at zero magnetic field stands in contrast to the Coulomb diamonds measurement with a magnetic field of 500 mT (Fig. 3) applied in the plane of the sample, but not along the nanowire, to suppress superconductivity in the nanowire Al shell. In this case, the Coulomb peaks have the same periodicity and a significant height even at zero DC bias.

From the measurements presented in Figs. 2 and 3, we infer $1e$ periodicity of the Coulomb blockade at zero magnetic field. Moreover, we interpret that at zero magnetic field the left side of the device can exchange both single electrons and (Cooper) pairs with the neighboring lead, while the right side can only exchange electron pairs [Fig. 2(d)]. In particular, the suppression of conductance at zero DC bias in Fig. 2(c) can be explained as follows. Zero-bias conductance through the right end of the island can only occur if N and $N + 2$ occupancy of the island are degenerate [brown squares in Fig. 2(e)]. However, the single electrons can be easily exchanged with the left lead. Consequently, when the N and $N + 2$ occupancies are degenerate, the island is in $N + 1$ occupancy and exchange of the electron pairs with the right lead remains impossible. This blockade is lifted in magnetic field (Fig. 3) when aluminum becomes normal and both ends of the island can exchange single electrons with both leads when occupancies different by one are degenerate [green circles in Fig. 2(e)].

To complete the low-frequency characterization of the device, in Fig. 4 we study the superconducting gap closing on the right side of the device A as a function of the magnetic

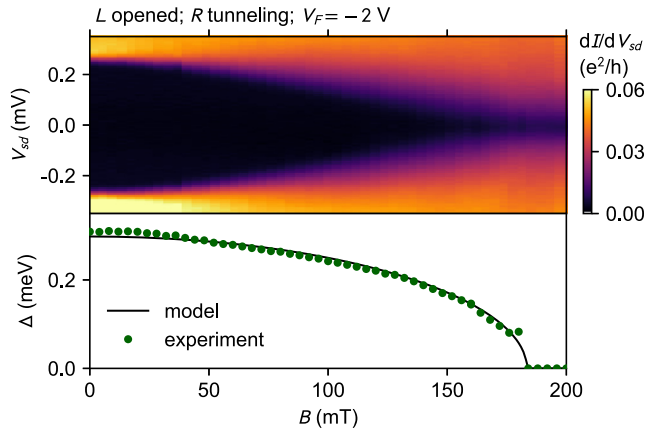


FIG. 4. Tunneling spectroscopy of the superconducting gap at the filtered end of the main island as a function of external magnetic field B applied approximately 20° away from the wire direction. Bottom panel shows the extracted superconducting gap Δ . The fit of Eq. (1) to the data, presented with a solid line, was used in the further analysis of poisoning rates in the external magnetic field. Data for device A.

field B (applied in the plane of the device, approximately 20° away from the wire direction). The bottom panel of Fig. 4 shows extracted gap size Δ as a function of B . The dependence $\Delta(B)$ is well described by the formula [53]

$$\Delta(B) = \Delta_0 \sqrt{1 - (B/B_c)^2}, \quad (1)$$

where $\Delta_0 = 308 \pm 2 \mu\text{eV}$ is the fitted superconducting gap at zero field and $B_c = 183 \pm 1 \text{ mT}$ is the fitted critical field (see Appendix A for more details of the fitting procedure). These measurements will serve as a reference in the study of the main island poisoning at finite magnetic field in Sec. VI.

IV. RF CHARGE STABILITY DIAGRAM OF THE ISLAND

Next, voltages of the barrier gates are adjusted to study the efficiency of the quasiparticle filter. The voltage of the left barrier gate is set below $V_L = -1 \text{ V}$ to prevent any tunneling into the island (see Appendix B) directly into the $1e$ region [through the barrier L in Fig. 1(b)]. For comparison, the conductance saturates at maximum value for $V_L = 200 \text{ mV}$ and becomes unmeasurable at $V_L = -300 \text{ mV}$. Meanwhile, the right barrier gate, neighboring the filter, is operated in the tunneling regime, in range $V_R = -80$ to -250 mV . The filter gate voltage V_F is set to -4 V to create a hard gap in the filter region [51].

Figure 5 presents two charge diagrams of the main island as a function of two barrier gate voltages, swept in the same range but with different acquisition rates. The range within which the barrier gate voltages are changed does not significantly affect tunneling rates between the island or any of the leads. Figure 5(a) presents the rf charge-sensing signal measured with a digital multimeter and an integration time of 20ms. The panel below the charge diagram shows a cut through the data, revealing a characteristic staircase shape [54,55]. Each step indicates a charge degeneracy point at

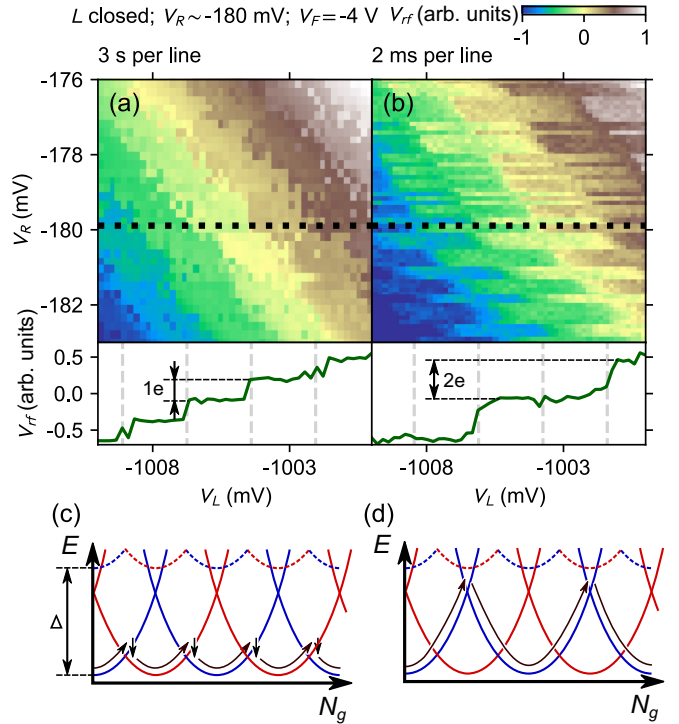


FIG. 5. Charge diagrams of the main island with the left barrier fully pinched off at $V_L \approx -1 \text{ V}$ and right in the tunneling regime at $V_R \approx -180 \text{ mV}$. Filter gate voltage is set to $V_F = -4 \text{ V}$. Demodulated rf charge sensing signal was measured with (a) a digital multimeter and averaging time of 20 ms; (b) a waveform digitizer synchronized to 1.903 kHz sawtooth waveform applied to V_L , with 4 averages per line. Bottom panels of (a) and (b) present cuts through the data to illustrate the different periodicity of the charge-sensing staircase. (c), (d) Schematic explanation of different observed periodicities of the staircase. The curved arrow follows the energy of the lowest charge state and the downward arrow in (c) represents a poisoning event. In (a) and (c), the poisoning time is faster than the acquisition rate, allowing for the relaxation to the charge state with lowest energy, independently of its parity. In (b) and (d), the sweeping rate is faster than the poisoning rate and thereby the parity of the island is fixed within each horizontal cut. Data for device B.

which a single electron is added or removed from the island, while plateaus indicate that the charge is fixed.

Figure 5(b) shows the same measurement taken at a faster rate. We apply a 1.903 kHz sawtooth wave form to V_L and measure the charge sensing signal using a synchronized waveform digitizer [56]. Each row in the data is an average over four periods of the sawtooth. In this way, every row is acquired within 2 ms and averaging time per point is $22 \mu\text{s}$. An example of a single row (cut through the data) is shown in the bottom panel. With the increased acquisition rate, we observe irregular switching between two staircase shapes offset by half a period relative to each other and with twice the period of the staircase in Fig. 5(a) (as illustrated with dashed vertical lines).

Our interpretation is that, in case of Fig. 5(a), the data is acquired at rates slower than the poisoning time from the right lead. As a consequence, we always measure the charge on the island corresponding to its ground-state occupancy, Fig. 5(c). Since the left barrier of the island is fully closed, the

quasiparticles that poison the island must come from the right lead and pass the filter region to the soft-gapped $1e$ region.

On the contrary, measurement speed for data in Fig. 5(b) exceeds the poisoning rate. Since the gap size ($\Delta_0 \approx 0.25$ meV for device B) exceeds twice the charging energy of the island ($E_c \approx 0.1$ meV), only electron pairs can be added to the island from the right lead on the relevant timescale, doubling the staircase period [Fig. 5(d)].

The contrast between these two data sets makes evident that the poisoning occurs at a timescale between the acquisition time of the data in Figs. 5(a) and 5(b), i.e., tens of milliseconds (corresponding to switching rate of hundreds of s^{-1}). Meanwhile, the doubled periodicity of the staircase in Fig. 5(b) establishes that the tunneling rate of the electron pairs remains much larger than the sawtooth frequency of 1.903 kHz. At this stage, we can not determine the mechanism of the poisoning from the right lead but further measurements (Sec. VI) demonstrate it originates from the electron tunneling through the gapped region rather than the electrons being thermally excited above the superconducting gap.

We dedicate the remainder of the paper to quantifying $2e$ -switching and $1e$ -switching (poisoning) rates as a function of various control knobs. Large tunability of these rates and orders-of-magnitude difference between them are the key findings of this paper.

V. QUANTIFYING POISONING RATE

To quantify the poisoning rate and $2e$ -switching rate, the voltage on the filter gate V_F and right barrier gate V_R was fixed while keeping the left barrier gate V_L at a large negative voltage, ranging between -1 and -5 V. Next, V_L was varied

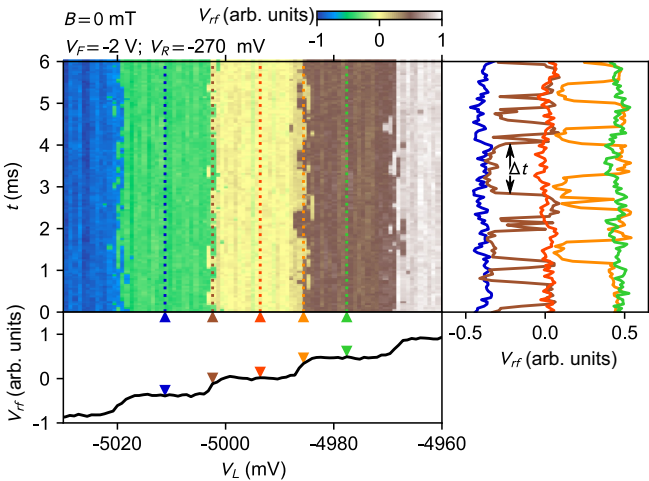


FIG. 6. Example of time traces used in the analysis of the switching rate. The two-dimensional color map shows the time vs gate charge signal corrected from its slope (caused by the slope of the sensor's Coulomb peak) to reveal individual charge steps. The bottom panel shows the gate dependence of time-averaged rf charge sensing signal. The right panel shows selected time traces extracted from the main two-dimensional color plot, for values of V_L indicated with dotted lines and triangular markers. Statistics of the waiting times Δt between switching events witnesses the poisoning rate of the island. Data for device B.

within a small range over which the occupancy of the main quantum dot changed by only a few electrons, thus using the barrier gate as a plunger in that instance. For each value, we acquired a time trace of the signal from the rf charge sensor [48] as illustrated in Fig. 6, which shows 6-ms-long time traces for $V_F = -2$ V and $V_R = -270$ mV. For most values of V_F , the occupancy of the dot was stable, with the exception of the vicinity of charge transitions, which showed $1e$ switching. Time traces obtained at the charge transition and in the stable region are presented in the right panel of Fig. 6. The corresponding values of V_L are indicated with triangular markers in the bottom panel.

We focus on voltages V_L in the vicinity of the charge transition and analyze the corresponding time traces in two ways. First, for each voltage V_F , we generate a histogram of the rf charge sensor measurements. The resulting distribution is typically bimodal, as shown in Fig. 7(a), and well fitted by a double Gaussian. The two modes correspond to two occupancies of the main island differing by one electron. As demonstrated in Fig. 7(b), the counts shift between the two modes across a charge transition. We model the probability of detecting charge states N and $N + 1$ by a thermal occupation

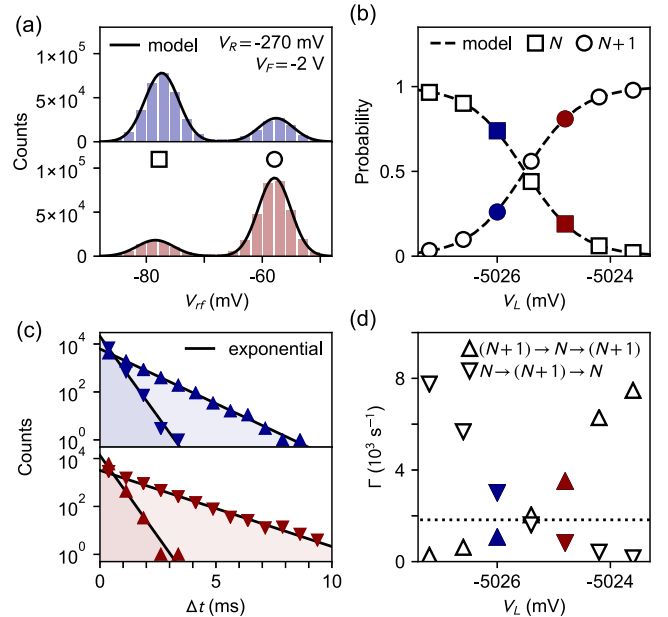


FIG. 7. (a) Histograms of rf charge sensing signal for $V_R = -270$ mV, $V_F = -2$ V, and $B = 0$ mT at two different values of V_L (in blue, before the charge transition and in red, after the charge transition). (b) Probability of finding an island in certain charge state in the vicinity of the charge transition. Dashed lines are fit of the Eq. (2) to the data. (c) Histograms of the waiting times Δt between subsequent poisoning events (cf. Fig. 6). Triangles pointing up/down indicate electrons tunneling into/out of the island. Solid lines are exponential fits to the data. (d) Switching rates in the vicinity of the charge transition extracted from the exponential fits as in (c). Dotted line indicates $\Gamma = \Gamma_{in}(V_L) = \Gamma_{out}(V_L)$. Colored markers in (b) and (d) indicate V_L , corresponding to data sets in (a) and (c). Data for device B.

of the island as

$$P_N = \frac{e^{-(N-N_g-\frac{1}{2})^2 E_c/k_B T}}{e^{-(N-N_g-\frac{1}{2})^2 E_c/k_B T} + e^{-(N-N_g+\frac{1}{2})^2 E_c/k_B T}},$$

$$P_{N+1} = 1 - P_N, \quad (2)$$

where $N_g = \alpha(V_L - V_L^0)$ is a gate-induced charge, with lever arm α and V_L^0 voltage offset; E_c is the island charging energy, k_B is the Boltzmann constant and T is the electron temperature. The two-parameter fit ($V_L^0 = 5025.509 \pm 0.005$ mV and $\alpha E_c/k_B T = 0.486 \pm 0.005$ mV⁻¹) results in a very good agreement with the data.

We now study the characteristic poisoning time. Figure 7(c) presents the histogram of time differences Δt between consecutive switches (i.e., time periods over which the charge of the island is fixed). In both cases, the distribution of time between switching events is exponential. In this way, statistics of switching for a specific V_L can be fully characterized by a rate of the electron tunneling in (Γ_{in}) and out (Γ_{out}). Figure 7(d) presents the change of the tunneling rates across the charge transition. To analyze the filter efficiency, we need to exclude poisoning protection by charging energy [48]. These effects do not play a role when the chemical potential of the island is aligned with the Fermi level of the lead and, thereby, as a poisoning measure, we choose the switching rate at gate voltage V_L for which $\Gamma_{\text{in}} = \Gamma_{\text{out}} \equiv \Gamma$, indicated by a dotted line in Fig. 7(d). This condition is equivalent to the island spending an equal amount of time in the two occupancies. The analysis described in this section underlies each of the Γ measurements in the following discussion.

VI. FILTER EFFICIENCY

Having established a quantitative measure of the poisoning rate, we study its dependence on the filter gate V_F and the right barrier gate voltage V_R . One should note that the voltages indicated for the different gates at a given conductance value can vary between measurements due to hysteresis, as explained more thoroughly in Appendix B. We correlate poisoning rates with conventional zero-bias DC measurements across the right barrier. Figure 8(a) presents the conductance through the barrier as a function of V_F and V_R , measured by rf reflectometry. For most negative V_F , between -4 to -1.5 V, there is a weak dependence on V_F , aside from a weak cross-talk effect resulting in a small negative slope. For V_F between -1.5 and 0 V, we observe a smooth step, lowering the voltage for a complete pinch-off, using V_R by approximately 50 mV. For V_F above 0 V, the right barrier gate voltage must be significantly more negative to fully block conductance. The nearly vertical features seen at more positive $V_F \approx 0$ can be attributed to an unintentional quantum dot in the barrier [9,57].

Our interpretation of the data between $V_F = -4$ and -1 V is that the semiconducting part of the wire below the filter gate is maximally depleted and strongly coupled to the superconductor [37,41,42,51,58]. For more positive V_F , carriers are accumulated in the semiconductor.

We find that quasiparticle tunneling rates agree with this interpretation. Figure 8(b) presents the tunneling rates Γ

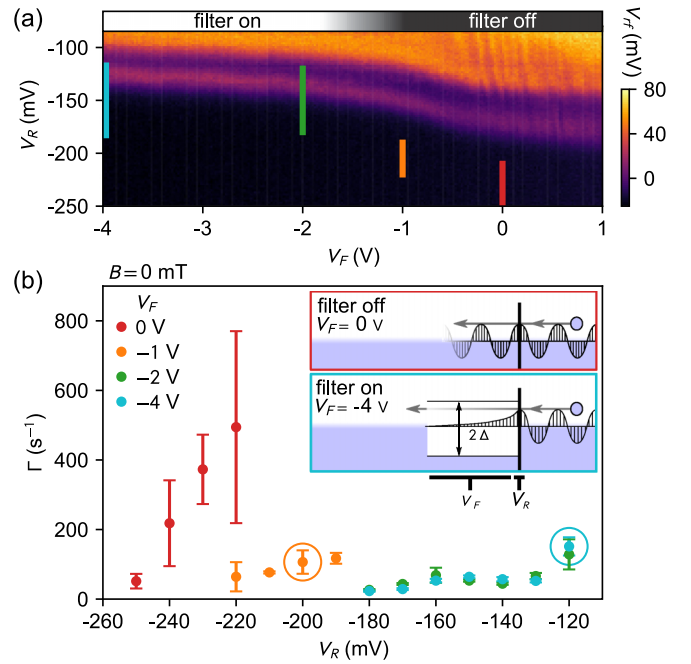


FIG. 8. (a) Differential conductance through the right barrier of the main island, with the left barrier fully opened, as a function of V_R and V_F at $V_{sd} = 0$, measured by means of rf reflectometry. (b) Dependence of the poisoning rate on V_R for various filter gate voltages V_F and for fully closed V_L . The corresponding regions in gate voltage space are indicated by vertical lines in (a). The inset shows the physical mechanism of quasiparticle filtering. When the filter is off (red-framed inset), an incident electron from the right lead needs only to tunnel through the barrier to poison the island. When the filter is on (blue-framed inset), an electron needs to tunnel through both: Barrier and $1\text{-}\mu\text{m}$ -long superconducting region with gap Δ . The raw data behind the points indicated with circles of respective colors was analyzed also with an alternative method, as described in Sec. VII. Data for device B.

obtained at the charge degeneracy points for several values of V_F and V_R . Colored lines in Fig. 8(a) indicate corresponding positions in the color map. For all values of V_F , tunneling rates decrease with decreasing voltage V_R . This dependence can be easily understood considering that the barrier gate voltage V_R changes the transparency of the normal-superconducting interface at the position of the right barrier and suppresses quasiparticle poisoning. However, this suppression reduces both single-electron and electron-pair tunneling and does not result in quasiparticle-filtering properties. On the other hand, decreasing the filter gate voltage V_F disproportionately affects the $1e$ tunneling rate. As demonstrated in Fig. 8(b), the single electron tunneling rate for $V_F = -2$ V is below 200 s⁻¹ in the entire studied range of V_R , between -180 and -120 mV (for more positive V_R the charge sensing signal disappears due to strong $2e$ quantum fluctuations, see Sec. VII). To achieve the same tunneling rate with $V_F = 0$, V_R has to be decreased to -250 mV. As illustrated with colored lines in Fig. 8(a), this is a disproportional change relative to the 50 mV shift of the pinch-off curve between $V_F = -2$ and 0 V. At the same time, a decrease of V_F from -2 to -4 V has virtually no impact on

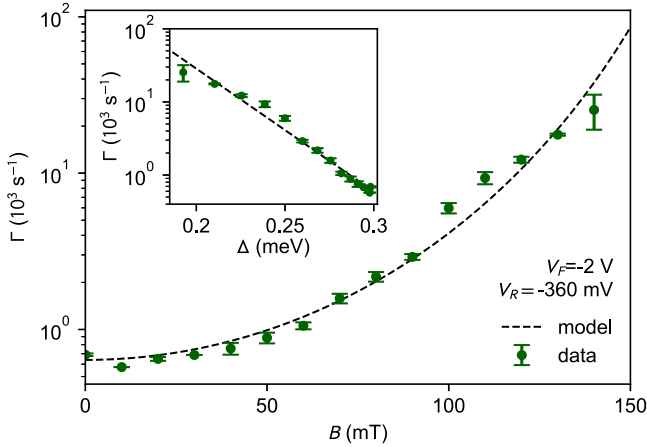


FIG. 9. Field dependence of the poisoning rate for $V_F = -2$ V, $V_R = -360$ mV. The dashed line is a model fit to the data using the field dependence of the superconducting gap $\Delta(B) \propto 1/\xi(B)$ fitted to the data in Fig. 4(a). For a description of the model, see the main text. The inset shows the poisoning rates as a function of superconducting gap size $\Delta(B)$. Data for device A.

the poisoning rates, consistent with reaching a maximum in the proximity coupling of semiconducting states [41,42,58].

Our interpretation of these observations is illustrated in the insets of Fig. 8(b). When the voltage $V_F < -2$ V, the semiconductor of the gated nanowire segment is depleted sufficiently to have a hard gap and, to poison the island, quasiparticles must tunnel through a $1\text{-}\mu\text{m}$ -long region with gap Δ (blue-framed inset). On the other hand, when $V_F \geq 0$, the semiconductor is not depleted and quasiparticles only have to tunnel through the barrier junction (red-framed inset).

Next we study whether applying an external magnetic field influences the poisoning rate. Figure 9 shows the magnetic field dependence of the poisoning rate for $V_F = -2$ V and $V_R = -360$ mV in device A (different from the one discussed in Fig. 8). The poisoning rate increases as the magnetic field that suppresses the gap of the filter.

We model poisoning processes as limited by single-particle tunneling through the filter,

$$\Gamma = Ae^{-L/\xi(B)}, \quad (3)$$

where A is the tunneling rate excluding the superconducting filter and $L = 1 \mu\text{m}$ is the length of the quasiparticle filter. The magnetic-field dependence of the coherence length $\xi(B)$ can be modeled within BCS theory as $\xi(B) = \hbar v_F / \pi \Delta(B)$ where v_F is the Fermi velocity and $\Delta(B)$ is obtained from the DC measurement in Fig. 4(a). Specifically, we use the relation $L/\xi(B) = \Delta(B)/b$, where b is a fit parameter (with $b = \hbar v_F / \pi L$ for the clean case in BCS theory). Using this model and data from Fig. 4(b), we fit the field dependence of Γ in Fig. 9. We find that $A = 66 \pm 28 \times 10^6 \text{ s}^{-1}$ and $b = 26 \pm 1 \mu\text{eV}$ yields a good matching with the data for poisoning rates ranging two orders of magnitude. The value of b is significantly larger than $k_B T \approx 4 \mu\text{eV}$, which suggests that the field dependence of the tunneling rate cannot be explained by thermally activated quasiparticles crossing the filter but rather by quantum tunneling. The corresponding coherence length is $\xi(0) = 90 \pm 10 \text{ nm}$, taking into account a 50-nm

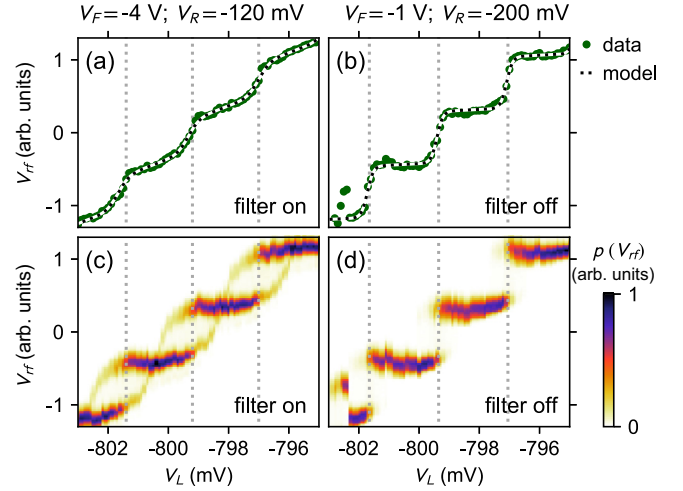


FIG. 10. Charge steps measured with quasiparticle filter on (a) and (c) and off (b) and (d). Panels (a) and (b) show the averaged time traces, as in Fig. 6, fitted by formula in Eq. (4). Panels (c) and (d) show histograms of charge sensing signal, as in Fig. 7(a), as a function of V_L . Data for device B.

uncertainty in the length of the filter (accounting for the size of the barrier gates). This value of ξ at zero magnetic field is one order of magnitude smaller than that of bulk Al (1600 nm) and a factor of $2\text{--}3$ smaller than the inferred coherence length in topological regime in Refs. [5] (260 nm) and [6] (180 nm).

VII. QUANTUM CHARGE FLUCTUATIONS IN PRESENCE OF QUASIPARTICLE FILTERING

In this section, we demonstrate that the quasiparticle filter allows for maintaining a low poisoning rate while simultaneously having strong coupling to the lead, as indicated by transition broadening due to $2e$ quantum charge fluctuations. For that purpose, we reanalyze two of the data sets, adjusted to have comparable poisoning rates but corresponding to different settings of the barrier gate voltage V_R . To achieve comparable poisoning rates, the data set in the regime of the active filter (filter on) is operated with the right cutter in the open regime while, for the other data set, in the filter-off regime, the right cutter is almost closed. The corresponding data points are indicated by the circles in Fig. 8 and are characterized by poisoning rates of $\Gamma_{\text{on}} = 151 \pm 26 \text{ s}^{-1}$ and $\Gamma_{\text{off}} = 106 \pm 34 \text{ s}^{-1}$ for on and off cases, respectively.

Time-averaged charge sensing signal for these two data sets is presented in Fig. 10(a) and Fig. 10(b) as a function of V_L with green points. In both cases, we observe a characteristic staircase shape. However, the steps are much more pronounced when the filter is off relative to the filter-on configuration. In both cases, the periodicity corresponds to $1e$ charging effects. In the following we test the consistency of the data with an exclusively thermal broadening of the charge transitions. Below we demonstrate that this model holds well in the filter off case but fails in the filter on case.

For purely thermal broadening, the time-averaged charge is given by the thermodynamic expectation value:

$$\langle Q \rangle = e \times \frac{\sum_n n \exp(-(n - N_g)^2 E_c / k_B T)}{\sum_n \exp(-(n - N_g)^2 E_c / k_B T)}. \quad (4)$$

Taking the charge sensor sensitivity and direct crosstalk between gate V_L and the sensor into account, a fit of Eq. (4) to the data yields $E_c/k_B T = 6.3 \pm 1.0$ and 11.7 ± 1.0 for filter on and off cases, respectively. The result is plotted in Fig. 10(a) and Fig. 10(b) with black dotted lines. We interpret the difference as an indication of charging energy renormalization.

Next, we generate histograms of charge sensor measurements separately for each of the time traces taken at different V_L , as in Sec. V and Fig. 7(a). The histograms for various V_F are plotted as a color map in Fig. 10(c) and Fig. 10(d). In the filter-off case [(d)], the distribution is unimodal, except in the vicinity of the charge transition. We attribute this to the stability of a single charge state whenever Coulomb blockade suppresses poisoning. Meanwhile, when the filter is on, the distribution is always bimodal, corresponding to two distinct charge states. From this, we conclude that the two lowest charge states must always differ in energy by not much more than $k_B T$, otherwise the probability of finding the system in the excited state would be negligible. This corroborates the factor-of-2 difference in $E_c/k_B T$ obtained from the fit in Fig. 10(a) and Fig. 10(b).

More intriguingly, the mode corresponding to the excited state never disappears. Instead, the mode corresponding to a charge state N continuously shifts to a position corresponding to a charge $N \pm 2$. We consider two alternative explanations of these superimposed and shifted $2e$ steps. First, it is possible that the $2e$ tunneling rate exceeds significantly the temporal resolution of the charge sensor while $1e$ tunneling rate is within our temporal resolution. In such case, we detect the time-averaged charge with fixed parity. Alternatively, it is possible that we observe quantum charge fluctuations that cause the charge of the island to be noninteger [59–61].

To distinguish between those possibilities, we process the data in Fig. 10(c) by fitting double Gaussian distributions to each of the histograms to obtain the charge sensing signal corresponding to both detected charge states as well as the probability of detecting each of them. The result of this procedure is plotted in Fig. 11 and tested against the two hypothesis.

To test the hypothesis of thermal broadening, we fit Eq. (4) using only n -even or only n -odd, simultaneously to the positions of the two modes. Leaving $E_c/k_B T$ free allows for a good fit to the data, presented with the dashed line in Fig. 11. However, the obtained value of $E_c/k_B T = 1.7 \pm 0.2$ is a factor of 4 smaller than the value $E_c/k_B T = 6.3 \pm 0.7$ obtained earlier for the same data set from the fit in Fig. 10(a). Alternatively, a fixed value of $E_c/k_B T = 6.3$ results in a poor agreement with the data, presented with the dotted line in Fig. 11. We conclude that the observed behavior can not be explained in terms of thermal broadening.

For a description of quantum charge fluctuations we employ the model developed in Ref. [60] to quantify the coupling strength between the island and the normal lead. The main island of our device is treated as a superconductor coupled

to a normal lead. The coupling strength is then quantified in terms of the normal reflection coefficient r at the interface. Assuming that the coupling is to a single channel, for $r \ll 1$, the ground-state energy of the island is then given (to the second order in r) by

$$E_{GS} = -\sqrt{E_c \Delta_0} r \cos(\pi N_g) - E_c r^2 \ln \left(\frac{E_c}{\Delta_0} \right) \cos^2(\pi N_g), \quad (5)$$

where Δ_0 is the superconducting gap of the filter at $B = 0$ and $E_c = 0.08$ meV is the bare charging energy of the island (not taking into account the renormalization due to quantum fluctuations). E_c is extracted from several Coulomb diamond measurements in both normal and superconducting states of the Al shell. This model predicts [60] the mean charge of the island to be

$$Q(N_g) = e N_g - \frac{e}{2E_c} \frac{\partial E_{GS}}{\partial N_g}. \quad (6)$$

As previously, we supplement this formula with the charge sensor sensitivity and direct crosstalk between gate V_L and the sensor. Next, we perform simultaneous fits of $Q(N_g)$ and $Q(N_g + 1)$ to the extracted positions of the two modes. The result is plotted in Fig. 11 with a solid line. The fit yields a normal reflection coefficient of $r = 0.1 \pm 0.04$, corresponding to dimensionless conductance $g = 1 - r^2 = 0.99 \pm 0.01$. This value for the conductance indicates that in the filter on case, the coupling to the lead is very strong while still keeping very low poisoning rates.

We note that the close-to-perfect transmission obtained from the single-channel fit indicates that while quantum charge fluctuations are strong, the single-channel model likely does not apply in our experiment. Instead, the island is rather to be coupled to multiple channels in the normal leads. To the best of our knowledge, there is no analytical formula

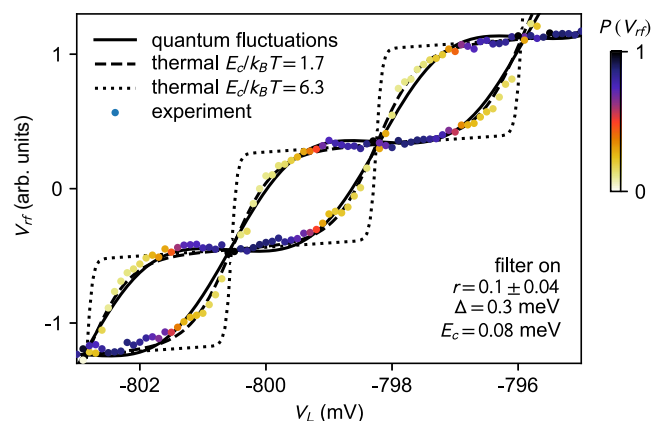


FIG. 11. Extracted positions and amplitudes of peaks of histograms presented in Fig. 10(c). The solid line is the model of quantum charge fluctuations fitted to the data. Superconducting gap $\Delta = 0.3$ meV and charging energy $E_c = 0.08$ meV used in the model were measured independently. The simultaneous fit of the two presented curves yields a reflection coefficient of $r = 0.10 \pm 0.04$. Dashed and dotted lines present predictions of the thermal model (see text) for $E_c/k_B T = 1.7$ and 6.3 , respectively. Data for device B.

for the expected scenario that includes more than the first-order approximation in $1 - g$. However, we do not expect the charge steps to take significantly different shapes from the one assumed above.

VIII. CONCLUSIONS

To summarize, we studied the poisoning rate of gapless states in a nanowire island that are separated from a quasiparticle reservoir (normal lead) by a hard-gap superconducting segment of the island (filter). By means of radio-frequency charge sensing, we directly probe the poisoning events.

Poisoning rates that are consistent with tunneling through a $1\text{-}\mu\text{m}$ -long (length of our quasiparticle filter) barrier of the height of the induced superconducting gap $\Delta(B)$. The efficiency of the filter is highly tunable by electrostatic gating of the filter section. The single electron tunneling rates can be as low as $\Gamma_{\text{on}} = 151 \pm 26 \text{ s}^{-1}$, while the coupling to the normal lead is sufficiently strong to observe $2e$ quantum charge fluctuations. Moreover, according to our interpretation, the quasiparticle poisoning rate could be exponentially suppressed by increasing the length of the quasiparticle filter.

The measured tunneling rate is midway between the corresponding parity lifetimes reported in Refs. [22,25], which can be treated as limiting cases of infinite-length and length-zero filter. The former [25] examines an InAs island with epitaxial Al with normal lead and, in the strong coupling limit, estimates $\sim 1 \mu\text{s}$ parity lifetime. Meanwhile, the latter [22] finds a parity lifetime of the NbTiN single electron transistor with Al leads approaching a minute timescale.

These results demonstrate that a quasiparticle filter based on the tunability of the superconducting gap has been realized.

ACKNOWLEDGMENTS

We thank S. Upadhyay for contributions to device fabrication and F. Kueemeth for contributions to the experimental setup. We also thank R. Lutchyn for fruitful discussions. Research was supported by Microsoft, the Danish National Research Foundation, and the European Commission.

APPENDIX A: MAGNETIC FIELD DEPENDENCE OF THE SUPERCONDUCTING GAP

To extract the gap from the raw data, we perform a fit of each spectrum. This is performed by convolving the Fermi-Dirac distribution at temperature T with the following formula for the raw gap [62]:

$$\rho(E) = \Re \left(\frac{E + i\gamma}{\sqrt{(E + i\gamma)^2 - \Delta^2}} \right), \quad (\text{A1})$$

where γ is a phenomenological parameter describing the finite in-gap conductance. E is the applied voltage bias and Δ is the superconducting gap we want to extract.

To perform the fit, we fix the temperature $T = 55 \text{ mK}$ and the phenomenological parameter $\gamma = 0.01 \text{ meV}$ as extracted from the zero field data. These values are obtained together with a value of the gap at zero field $\Delta_0 = 0.3 \text{ meV}$. We then proceed in fitting the gap with these fixed parameters at various values of the magnetic field. The resulting values

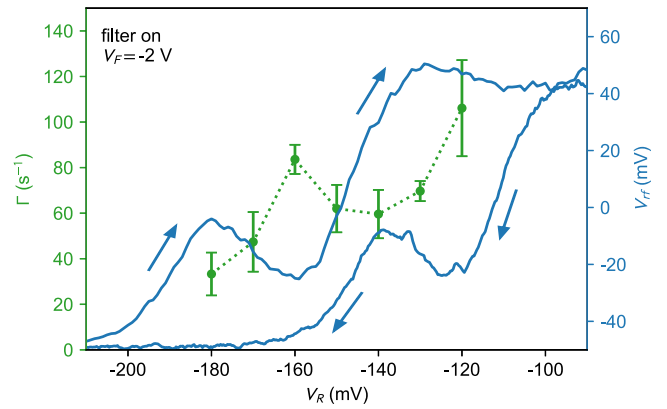


FIG. 12. Right barrier characterization for device B. The blue curves show the reflectometry signal in both up and down sweeps of the right barrier. The poisoning rate extracted at $V_F = -2 \text{ V}$ is overlaid as a comparison to the conductance pinch-off.

of $\Delta(B)$ are plotted with dots on Fig. 4(b). To eliminate the fluctuations and the nonmonotonicity inherent to that type of procedure, we then fit the extracted $\Delta(B)$ dependence to the BCS gap from Eq. (1), leading to a critical field of $183 \pm 1 \text{ mT}$.

APPENDIX B: BARRIERS CHARACTERIZATION

To supplement our discussion about the relation between the pinch-off of the tunneling barriers and the poisoning rate, we present in Fig. 12 the up and down pinch-off curve from the right barrier. These curves clearly show the hysteresis of the barriers. This hysteresis prevents us from presenting a direct correlation between the poisoning rate and the zero and high-bias conductance that are obtained in a completely different configuration of the barrier gates.

The pinch-off point of the conductance through the right barrier is obtained for a voltage $V_R \simeq -170 \text{ mV}$ when sweeping from positive to negative voltages. When sweeping in the opposite direction, the pinch-off can be obtained around a voltage $V_R \simeq -210 \text{ mV}$. The hysteresis for the pinch-off of the right barrier is thus of approximately $\Delta V_R = 40 \text{ mV}$. On top of these two curves, we superpose the poisoning rate obtained in the same filter on configuration at $V_F = -2 \text{ V}$. A correlation between the pinch-off curves and the poisoning rate can be observed. However, due to hysteresis of the tunneling barriers (which causes the offset between the poisoning curve and the pinch-off curves), we were not able to simultaneously record the conductance signal and the poisoning rate. This complements our interpretation from the main text by suggesting that the poisoning rate is directly dependent on the value of the tunneling barrier.

We show in Fig. 13(a) the pinch-off curve obtained on the left barrier while having the right barrier completely open ($V_R = 1 \text{ V}$). The pinch-off point is obtained around $V_L \simeq -220 \text{ mV}$. However, despite losing all transport signal in this configuration, we show in Fig. 13(b) that the barrier value can still play a role in the charge transfer rate through the left side when the system is placed in a Coulomb blockade configuration. In these figures, the right side is kept at a

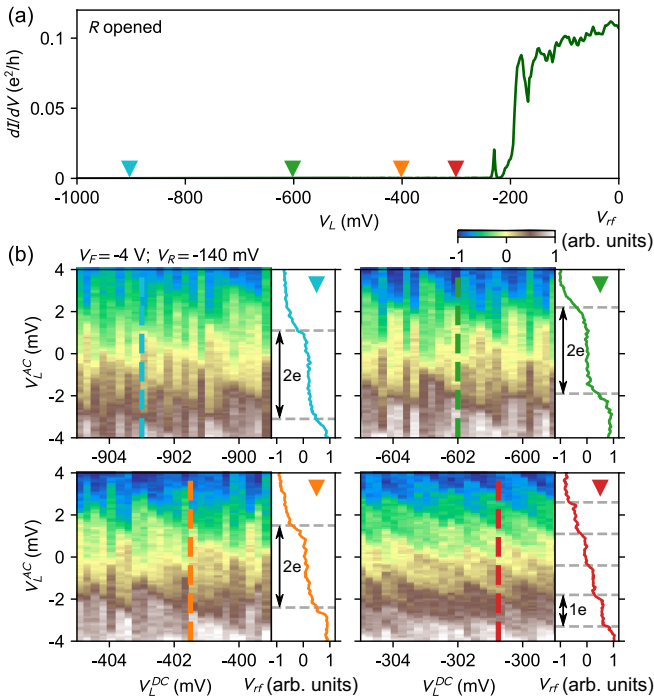


FIG. 13. Left barrier characterization for device B. Panel (a) shows the pinch-off curve of the left barrier in the range 0 to -1 V obtained by lock-in measurement while keeping the right side completely open. Panels in (b) show the charge steps acquired in reflectometry while varying the value of the left barrier and keeping it closed with respect to the pinch-off criterion. The x axis corresponds to slow sweeping of the barrier voltage while the y axis corresponds to an AC sawtooth excitation of the same gate. The barrier values at which these data sets were taken are indicated in (a) by colored triangles corresponding to the color of the side panels. These side panels show the typical charge steps taken in each of the configurations on which one can see the evolution from $1e$ charge steps to $2e$ charge steps as the barrier is turned more open.

voltage of -140 mV, corresponding to a near complete pinch-off as seen from Fig. 12.

When the left barrier is at its lowest voltage (blue triangle), the first panel of Fig. 13(b) shows that the Coulomb stairs are $2e$ periodic. This indicates that the poisoned part of the island is not able to exchange single electrons on the timescale of one sweep and that only paired electrons can penetrate the island through the right lead. This situation persists until the fourth panel (red), where we recover a situation of $1e$ periodicity of the charge steps. Such behavior is once again consistent with

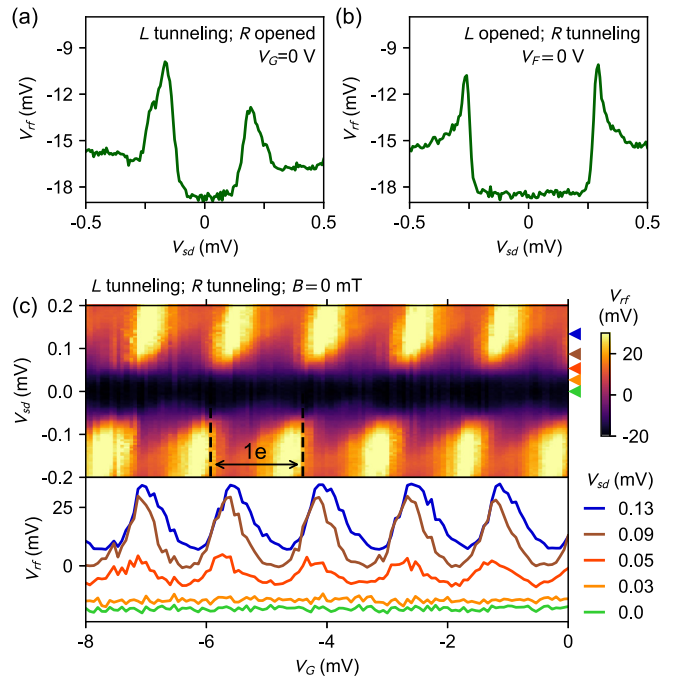


FIG. 14. Tunneling spectroscopy of the superconducting gap at the left (a) and right (b) ends of the main island for device B obtained by means of rf reflectometry. The inset text indicates the status of the left (L) and right (R) barriers. (c) Coulomb diamonds with very strongly suppressed zero bias conductance. Bottom panel shows cuts through the data at various V_{sd} .

tuning of a single electron tunneling to a poisoned side of the island by means of left barrier gate voltage V_L .

APPENDIX C: GAP SPECTROSCOPY IN DEVICE B

In Fig. 14, we present the spectroscopic measurement of the gap for both sides of the device B, similarly to gap measurements of device A in Fig. 2. Similar to device A, for device B we observe a clean and well-defined gap on the filter side [Fig. 14(b)], i.e., the side not covered by NbTiN. On the contrary, the gap of the $1e$ segment is reduced and softened [Fig. 14(a)]. This data is presented in units of voltage due to a lack of calibration between the reflectometry measurement and a standard lock-in measurement of the conductance for this device.

Furthermore, at zero magnetic field, we observe strong suppression of the zero-bias conductance [Fig. 14(c)], similar to device A.

- [1] S. Sachdev, *Quantum Phase Transitions* (Cambridge University Press, Cambridge, UK, 2011).
- [2] Z. Han, A. Allain, H. Arjmandi-Tash, K. Tikhonov, M. Feigel'man, B. Sacépé, and V. Bouchiat, *Nat. Phys.* **10**, 380 (2014).
- [3] J. Mooij, G. Schön, A. Shnirman, T. Fuse, C. Harmans, H. Rotzinger, and A. Verbruggen, *New J. Phys.* **17**, 033006 (2015).
- [4] C. G. L. Böttcher, F. Nichele, M. Kjaergaard, H. Suominen, J. Shabani, C. J. Palmström, and C. M. Marcus, *Nat. Phys.* **14**, 1138 (2018).
- [5] S. M. Albrecht, A. Higginbotham, M. Madsen, F. Kuemmeth, T. S. Jespersen, J. Nygård, P. Krogstrup, and C. M. Marcus, *Nature (London)* **531**, 206 (2016).
- [6] S. Vaitiekėnas, M.-T. Deng, P. Krogstrup, and C. M. Marcus, *arXiv:1809.05513*.
- [7] V. Mourik, K. Zuo, S. M. Frolov, S. R. Plissard, E. P. A. M. Bakkers, and L. P. Kouwenhoven, *Science* **336**, 1003 (2012).
- [8] A. Das, Y. Ronen, Y. Most, Y. Oreg, M. Heiblum, and H. Shtrikman, *Nat. Phys.* **8**, 887 (2012).

- [9] M. Deng, S. Vaitiekėnas, E. B. Hansen, J. Danon, M. Leijnse, K. Flensberg, J. Nygård, P. Krogstrup, and C. M. Marcus, *Science* **354**, 1557 (2016).
- [10] F. Nichele, A. C. C. Drachmann, A. M. Whiticar, E. C. T. O'Farrell, H. J. Suominen, A. Fornieri, T. Wang, G. C. Gardner, C. Thomas, A. T. Hatke, P. Krogstrup, M. J. Manfra, K. Flensberg, and C. M. Marcus, *Phys. Rev. Lett.* **119**, 136803 (2017).
- [11] G. C. Ménard, S. Guissart, C. Brun, R. T. Leriche, M. Trif, F. Debontridder, D. Demaille, D. Roditchev, P. Simon, and T. Cren, *Nat. Commun.* **8**, 2040 (2017).
- [12] H. Zhang, C.-X. Liu, S. Gazibegovic, D. Xu, J. A. Logan, G. Wang, N. van Loo, J. D. S. Bommer, M. W. A. de Moor, D. Car, R. L. M. Op het Veld, P. J. van Veldhoven, S. Koelling, M. A. Verheijen, M. Pendharkar, D. J. Pennachio, B. Shojaei, J. S. Lee, C. J. Palmström, E. P. A. M. Bakkers, S. Das Sarma, and L. P. Kouwenhoven, *Nature (London)* **556**, 74 (2018).
- [13] J. Chen, P. Yu, J. Stenger, M. Hocevar, D. Car, S. R. Plissard, E. P. Bakkers, T. D. Stanescu, and S. M. Frolov, *Sci. Adv.* **3**, e1701476 (2017).
- [14] G. de Lange, B. van Heck, A. Bruno, D. J. van Woerkom, A. Geresdi, S. R. Plissard, E. P. A. M. Bakkers, A. R. Akhmerov, and L. DiCarlo, *Phys. Rev. Lett.* **115**, 127002 (2015).
- [15] T. W. Larsen, K. D. Petersson, F. Kuemmeth, T. S. Jespersen, P. Krogstrup, J. Nygård, and C. M. Marcus, *Phys. Rev. Lett.* **115**, 127001 (2015).
- [16] F. Luthi, T. Stavenga, O. W. Enzinger, A. Bruno, C. Dickel, N. K. Langford, M. A. Rol, T. S. Jespersen, J. Nygård, P. Krogstrup, and L. Di Carlo, *Phys. Rev. Lett.* **120**, 100502 (2018).
- [17] L. Casparis, M. R. Connolly, M. Kjaergaard, N. J. Pearson, A. Kringhøj, T. W. Larsen, F. Kuemmeth, T. Wang, C. Thomas, S. Gronin, G. C. Gardner, M. J. Manfra, C. M. Marcus, and K. D. Petersson, *Nat. Nanotechnol.* **13**, 915 (2018).
- [18] D. Aasen, M. Hell, R. V. Mishmash, A. Higginbotham, J. Danon, M. Leijnse, T. S. Jespersen, J. A. Folk, C. M. Marcus, K. Flensberg, and J. Alicea, *Phys. Rev. X* **6**, 031016 (2016).
- [19] T. Karzig, C. Knapp, R. M. Lutchyn, P. Bonderson, M. B. Hastings, C. Nayak, J. Alicea, K. Flensberg, S. Plugge, Y. Oreg, C. M. Marcus, and M. H. Freedman, *Phys. Rev. B* **95**, 235305 (2017).
- [20] S. Plugge, A. Rasmussen, R. Egger, and K. Flensberg, *New J. Phys.* **19**, 012001 (2017).
- [21] J. Aumentado, M. W. Keller, J. M. Martinis, and M. H. Devoret, *Phys. Rev. Lett.* **92**, 066802 (2004).
- [22] D. J. Van Woerkom, A. Geresdi, and L. P. Kouwenhoven, *Nat. Phys.* **11**, 547 (2015).
- [23] J. van Veen, A. Proutski, T. Karzig, D. I. Pikulin, R. M. Lutchyn, J. Nygård, P. Krogstrup, A. Geresdi, L. P. Kouwenhoven, and J. D. Watson, *Phys. Rev. B* **98**, 174502 (2018).
- [24] M. Zgirski, L. Bretheau, Q. Le Masne, H. Pothier, D. Esteve, and C. Urbina, *Phys. Rev. Lett.* **106**, 257003 (2011).
- [25] S. M. Albrecht, E. B. Hansen, A. P. Higginbotham, F. Kuemmeth, T. S. Jespersen, J. Nygård, P. Krogstrup, J. Danon, K. Flensberg, and C. M. Marcus, *Phys. Rev. Lett.* **118**, 137701 (2017).
- [26] D. Rainis and D. Loss, *Phys. Rev. B* **85**, 174533 (2012).
- [27] E. T. Mannila, V. F. Maisi, H. Q. Nguyen, C. M. Marcus, and J. P. Pekola, *Phys. Rev. B* **100**, 020502(R) (2019).
- [28] J. M. Martinis, M. Ansmann, and J. Aumentado, *Phys. Rev. Lett.* **103**, 097002 (2009).
- [29] G. Catelani, R. J. Schoelkopf, M. H. Devoret, and L. I. Glazman, *Phys. Rev. B* **84**, 064517 (2011).
- [30] L. Sun, L. DiCarlo, M. D. Reed, G. Catelani, L. S. Bishop, D. I. Schuster, B. R. Johnson, G. A. Yang, L. Frunzio, L. Glazman, M. H. Devoret, and R. J. Schoelkopf, *Phys. Rev. Lett.* **108**, 230509 (2012).
- [31] D. Ristè, C. Bultink, M. Tiggelman, R. Schouten, K. Lehnert, and L. DiCarlo, *Nat. Commun.* **4**, 1913 (2013).
- [32] S. Gustavsson, F. Yan, G. Catelani, J. Bylander, A. Kamal, J. Birenbaum, D. Hover, D. Rosenberg, G. Samach, A. P. Sears, S. J. Weber, J. L. Yoder, J. Clarke, A. J. Kerman, F. Yoshihara, Y. Nakamura, T. P. Orlando, and W. D. Oliver, *Science* **354**, 1573 (2016).
- [33] A. Morpurgo, J. Kong, C. Marcus, and H. Dai, *Science* **286**, 263 (1999).
- [34] Y.-J. Doh, J. A. van Dam, A. L. Roest, E. P. Bakkers, L. P. Kouwenhoven, and S. De Franceschi, *Science* **309**, 272 (2005).
- [35] J. Shabani, M. Kjaergaard, H. J. Suominen, Y. Kim, F. Nichele, K. Pakrouski, T. Stankevic, R. M. Lutchyn, P. Krogstrup, R. Feidenhans *et al.*, *Phys. Rev. B* **93**, 155402 (2016).
- [36] P. Krogstrup, N. L. B. Ziino, W. Chang, S. M. Albrecht, M. H. Madsen, E. Johnson, J. Nygård, C. M. Marcus, and T. S. Jespersen, *Nat. Mater.* **14**, 400 (2015).
- [37] W. Chang, S. Albrecht, T. Jespersen, F. Kuemmeth, P. Krogstrup, J. Nygård, and C. M. Marcus, *Nat. Nanotechnol.* **10**, 232 (2015).
- [38] S. Gazibegovic, D. Car, H. Zhang, S. C. Balk, J. A. Logan, M. W. de Moor, M. C. Cassidy, R. Schmits, D. Xu, G. Wang, P. Krogstrup, R. L. M. Op het Veld, K. Zuo, Y. Vos, J. Shen, D. Bouman, B. Shojaei, D. Pennachio, J. Sue Lee, P. J. van Veldhoven, S. Koelling, M. A. Verheijen, L. P. Kouwenhoven, C. J. Palmström, and E. P. A. M. Bakkers, *Nature (London)* **548**, 434 (2017).
- [39] G. Goldstein and C. Chamon, *Phys. Rev. B* **84**, 205109 (2011).
- [40] J. C. Budich, S. Walter, and B. Trauzettel, *Phys. Rev. B* **85**, 121405(R) (2012).
- [41] A. E. G. Mikkelsen, P. Kotetes, P. Krogstrup, and K. Flensberg, *Phys. Rev. X* **8**, 031040 (2018).
- [42] A. E. Antipov, A. Bargerbos, G. W. Winkler, B. Bauer, E. Rossi, and R. M. Lutchyn, *Phys. Rev. X* **8**, 031041 (2018).
- [43] R. Schoelkopf, P. Wahlgren, A. Kozhevnikov, P. Delsing, and D. Prober, *Science* **280**, 1238 (1998).
- [44] M. Jung, M. Schroer, K. Petersson, and J. Petta, *Appl. Phys. Lett.* **100**, 253508 (2012).
- [45] K. Petersson, C. Smith, D. Anderson, P. Atkinson, G. Jones, and D. Ritchie, *Nano Lett.* **10**, 2789 (2010).
- [46] C. Barthel, M. Kjaergaard, J. Medford, M. Stopa, C. M. Marcus, M. P. Hanson, and A. C. Gossard, *Phys. Rev. B* **81**, 161308(R) (2010).
- [47] D. Razmadze, D. Sabonis, F. K. Malinowski, G. C. Ménard, S. Pauka, H. Nguyen, D. M. T. van Zanten, E. C. T. O'Farrell, J. Suter, P. Krogstrup *et al.*, *Phys. Rev. Appl.* **11**, 064011 (2019).
- [48] H. Nguyen, D. Razmadze, E. T. Mannila, V. F. Maisi, D. Sabonis, D. M. T. van Zanten, E. C. O'Farrell, P. Krogstrup, F. Kuemmeth, L. P. Pekola, and C. M. Marcus (unpublished).
- [49] O. Gül, H. Zhang, F. K. de Vries, J. van Veen, K. Zuo, V. Mourik, S. Conesa-Boj, M. P. Nowak, D. J. Van Woerkom, M. Quintero-Pérez *et al.*, *Nano Lett.* **17**, 2690 (2017).

- [50] Ö. Gül, H. Zhang, J. D. Bommer, M. W. de Moor, D. Car, S. R. Plissard, E. P. Bakkers, A. Geresdi, K. Watanabe, T. Taniguchi, and L. P. Kouwenhoven, *Nat. Nanotechnol.* **13**, 192 (2018).
- [51] S. Vaitiekėnas, M.-T. Deng, J. Nygård, P. Krogstrup, and C. M. Marcus, *Phys. Rev. Lett.* **121**, 037703 (2018).
- [52] R.-P. Riwar, A. Hosseinkhani, L. D. Burkhardt, Y. Y. Gao, R. J. Schoelkopf, L. I. Glazman, and G. Catelani, *Phys. Rev. B* **94**, 104516 (2016).
- [53] D. Douglass Jr, *Phys. Rev. Lett.* **6**, 346 (1961).
- [54] K. K. Likharev, *Proc. IEEE* **87**, 606 (1999).
- [55] D. S. Duncan, C. Livermore, R. M. Westervelt, K. D. Maranowski, and A. C. Gossard, *Appl. Phys. Lett.* **74**, 1045 (1999).
- [56] J. Stehlik, Y.-Y. Liu, C. M. Quintana, C. Eichler, T. Hartke, and J. Petta, *Phys. Rev. Appl.* **4**, 014018 (2015).
- [57] Y.-H. Lai, J. D. Sau, and S. D. Sarma, *Phys. Rev. B* **100**, 045302 (2019).
- [58] G. W. Winkler, A. E. Antipov, B. van Heck, A. A. Soluyanov, L. I. Glazman, M. Wimmer, and R. M. Lutchyn, *Phys. Rev. B* **99**, 245408 (2019).
- [59] M. V. Feigelman, A. Kamenev, A. I. Larkin, and M. A. Skvortsov, *Phys. Rev. B* **66**, 054502 (2002).
- [60] R. M. Lutchyn, K. Flensberg, and L. I. Glazman, *Phys. Rev. B* **94**, 125407 (2016).
- [61] S. Jezouin, Z. Iftikhar, A. Anthore, F. Parmentier, U. Gennser, A. Cavanna, A. Ouerghi, I. P. Levkivskiy, E. Idrisov, E. Sukhorukov, L. I. Glazman, and F. Pierre, *Nature (London)* **536**, 58 (2016).
- [62] R. C. Dynes, V. Narayanamurti, and J. P. Garno, *Phys. Rev. Lett.* **41**, 1509 (1978).